© 2018. Published by The Company of Biologists Ltd | Journal of Cell Science (2018) 131, jcs212654. doi:10.1242/jcs.212654

SHORT REPORT

Parallel assembly of actin and tropomyosin, but not myosin II, during *de novo* actin filament formation in live mice

Andrius Masedunskas[1], Mark A. Appaduray[1], Christine A. Lucas[1], María Lastra Cagigas[1], Marco Heydecker[1,2], Mira Holliday[1], Joyce C. M. Meiring[1], Jeff Hook[1], Anthony Kee[1], Melissa White[3], Paul Thomas[3], Yingfan Zhang[4], Robert S. Adelstein[4], Tobias Meckel[2], Till Böcking[1], Roberto Weigert[5], Nicole S. Bryce[1], Peter W. Gunning[1,]* and Edna C. Hardeman[1,]*

ABSTRACT

Many actin filaments in animal cells are co-polymers of actin and tropomyosin. In many cases, non-muscle myosin II associates with these co-polymers to establish a contractile network. However, the temporal relationship of these three proteins in the *de novo* assembly of actin filaments is not known. Intravital subcellular microscopy of secretory granule exocytosis allows the visualisation and quantification of the formation of an actin scaffold in real time, with the added advantage that it occurs in a living mammal under physiological conditions. We used this model system to investigate the *de novo* assembly of actin, tropomyosin Tpm3.1 (a short isoform of TPM3) and myosin IIA (the form of non-muscle myosin II with its heavy chain encoded by *Myh9*) on secretory granules in mouse salivary glands. Blocking actin polymerization with cytochalasin D revealed that Tpm3.1 assembly is dependent on actin assembly. We used time-lapse imaging to determine the timing of the appearance of the actin filament reporter LifeAct–RFP and of Tpm3.1–mNeonGreen on secretory granules in LifeAct–RFP transgenic, Tpm3.1–mNeonGreen and myosin IIA–GFP (GFP-tagged MYH9) knock-in mice. Our findings are consistent with the addition of tropomyosin to actin filaments shortly after the initiation of actin filament nucleation, followed by myosin IIA recruitment.

KEY WORDS: Actin, Tropomyosin, Intravital, Myosin II, Cytoskeleton, Assembly kinetics

INTRODUCTION

Animal cells contain two types of actin filaments; those containing only actin or, alternatively, those containing co-polymers of actin and tropomyosin (Tpm) (Gunning et al., 2015b; Lazarides, 1975, 1976). Studies in yeast (Johnson et al., 2014), flies (Goins and Mullins, 2015) and mammals (Bryce et al., 2003; Tojkander et al., 2011) have shown that the Tpm isoform determines the functional capacity of the filament (Gunning et al., 2015a). Multiple models, ranging from addition of Tpm after actin filament formation to co-polymerisation, could explain the formation of the actin–Tpm co-polymer (Holmes and Lehman, 2008; Wegner, 1979), but there is no experimental data to discriminate between these models.

Several ‘large-granule’ *in vitro* model systems have been used to investigate the initial assembly of actin filament structures (Jang et al., 2012; Miklavc et al., 2012, 2015; Nightingale et al., 2011; Sokac et al., 2003; Tran et al., 2015; Yu and Bement, 2007). Actin scaffolds encompassing the granules contain both branched and linear actin filaments (Porat-Shliom et al., 2013; Tran et al., 2015), similar to what is found in the cortical cytoskeleton and podosomes (Bovellan et al., 2014; Panzer et al., 2016). Here, we use the stimulation of secretory granule release in salivary gland acinar cells, where actin scaffold formation can be initiated by β-adrenergic receptor agonist application and then quantified in real time in live rodents using intravital subcellular microscopy (Masedunskas et al., 2011).

RESULTS AND DISCUSSION

Tpm3.1 is associated with actin filaments initiated around fusing secretory granules

Fig. 1A and Fig. S1A,B show a cross-section of a mouse salivary gland acinus expressing plasma membrane (PM)-localised tdTomato (mTomato) and Lifeact–GFP, which efficiently mark the PM of acinar cells (Muzumdar et al., 2007) and filamentous actin, respectively. Both subcellular markers outline the canaliculi into which secretory granules release their contents (arrowheads). mTomato rapidly transfers to the granule membrane upon fusion with the apical plasma membrane (APM) of the canaliculus (Masedunskas et al., 2011).

Fig. 1B shows the same region of the gland 5 min after stimulation of secretory granule fusion by subcutaneous injection of 0.01 mg/kg body weight isoproterenol. Arrows identify granules which have fused with the APM. Resting granules are not detectable because they are not associated with either mTomato or the actin polymer prior to fusion (Fig. 1A), as shown previously (Masedunskas et al., 2011). Granules that have fused with the APM display labelling with both mTomato and Lifeact–GFP (expanded views in Fig. 1B; Movie 1). Comparison of the kinetics of mTomato transfer to a granule membrane and Lifeact association with the single granule undergoing fusion shows that actin filament formation closely follows initial granule fusion with the plasma membrane (Fig. 1C; Movie 1). The initial increase in Lifeact–GFP fluorescence lags ∼1 s behind the mTomato signal increase (Fig. 1D; Fig. S1C).

The temporal relationship of actin filament formation and Tpm association with granule membranes was first studied by detecting the endogenous proteins. All granules engaged in APM fusion, as

---

[1]School of Medical Sciences, UNSW Sydney, NSW 2052, Australia. [2]Membrane Dynamics, Department of Biology, Technische Universität Darmstadt, Schnittspahnstrasse 3, 64287 Darmstadt, Germany. [3]South Australian Genome Editing, Facility Robinson Research Institute, University of Adelaide, Adelaide, SA 5005, Australia. [4]NHLBI, National Institutes of Health, Bethesda, MD 20892, USA. [5]Laboratory of Cellular and Molecular Biology, CCR, National Cancer Institute, Bethesda, MD 20892, USA.

*Authors for correspondence (e.hardeman@unsw.edu.au; p.gunning@unsw.edu.au)

A.M., 0000-0002-4533-5467; M.A.A., 0000-0002-4639-4039; M.H., 0000-0001-5813-8131; A.K., 0000-0001-8067-2656; T.M., 0000-0003-0759-2072; P.W.G., 0000-0003-0833-3128; E.C.H., 0000-0003-1649-7712

Received 30 October 2017; Accepted 12 February 2018

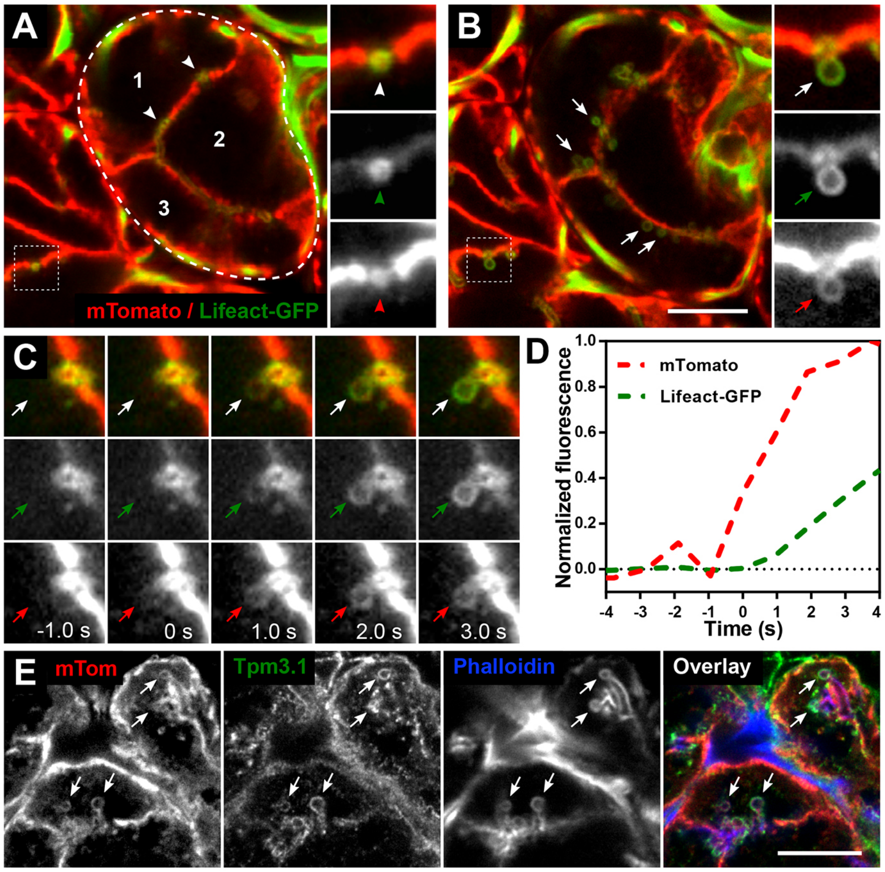

Fig. 1. *De novo* actin and Tpm 3.1 filament polymerisation forms a scaffold around granules after fusion with the APM. (A–D) Intravital confocal imaging of actin filament assembly during secretory granule exocytosis in submandibular salivary gland acinar cells in the progeny of an mTomato and Lifeact–GFP mouse cross. (A,B) Snapshots of salivary acini *in situ* showing the membrane marker mTomato (red) and F-actin marker Lifeact–GFP (green). (A) Snapshot was taken at a depth of 12 µm from the surface of the gland. Three individual acinar epithelial cells (numbers 1–3) are part of one acinus (encircled by dashed line). Actin is highly enriched at the APM/canaliculi (white arrowheads). Enlarged split channel images displayed on the right show an APM/canaliculus cross-section (red arrowhead) enriched with F-actin (green arrowhead). (B) The same area as in A was imaged 5 min after subcutaneous injection of isoproterenol. Granules fused to APM are seen (white arrows) after stimulation with isoproterenol. Enlarged split channel images show actin recruitment (green arrow) onto the fused granule as seen by the appearance of the mTomato membrane marker (red arrow). Scale bar: 10 µm; the width of the insets is 5.25 µm. See also Fig. S1 and Movie 1. (C) Enlarged time-course images of a representative granule fusion event. The granule acquires an mTomato signal at *t*=0 s, marking the fusion event (red arrows), and Lifeact–GFP is first detected around the granule circumference at *t*=1 s (green arrows). Each panel is 5.25 µm wide and the granule diameter is ∼1.2 µm; temporal sampling is 943 ms per frame. (D) Recruitment profiles of mTomato and Lifeact–GFP during a granule fusion event are shown as normalised fluorescence intensity over time. Increase in mTomato (red line) signal from baseline indicates fusion between the granule membrane and the APM. Increase in Lifeact–GFP (green line) indicates actin filament assembly. The frame before the first detection of actin polymerisation was set at *t*=0 s for this and all subsequent graphs. (E) Detection of mTomato, Tpm3.1 and actin (phalloidin) on fused granules (arrows) in a fixed salivary gland section from an mTomato mouse at 10 min after isoproterenol injection. The contrast was adjusted for each channel separately to facilitate consistent visualisation of the granules in all figures. Scale bar: 10 µm.

detected by mTomato transfer to the granules, displayed phalloidin staining (Fig. 1E). Co-staining for Tpm3.1 (a short isoform of TPM3) revealed that granules positive for phalloidin were also positive for Tpm3.1 (Fig. 1E). Almost all granules in the four mice displayed coincidence of phalloidin and Tpm3.1 (Table S1). The failure to detect many granules that are both phalloidin-positive and Tpm3.1-negative suggests that Tpm3.1 recruitment to the actin filament occurs at the same time as, or shortly after, actin assembly. Similarly, the failure to detect any granules that are both Tpm3.1-positive and phalloidin-negative is consistent with Tpm3.1 recruitment being dependent on the presence of actin filaments.

Tpm3.1 assembly requires actin, but actin assembly does not require Tpm3.1

Cytochalasin D, which disrupts actin polymer elongation (Cooper, 1987), was delivered into the salivary glands of mTomato mice via local perfusion. Alexa Fluor 647-labelled dextran, which does not enter the acinar cells, was used to track the presence of the drug solution and the location of cells exposed to it. Prolonged exposure to cytochalasin D results in dramatic swelling of the fused granules and inward blebbing of the APM, thus filling the cells with vacuoles (Masedunskas et al., 2011). Acinar cells further from the edge were less affected by the drug (Fig. 2A, green arrow). Acinar cells that were close to the edge of the organ contained granules with mTomato, indicating membrane fusion; however, the granules displayed a complete lack of phalloidin staining and, in parallel, no detectable Tpm3.1 (Fig. 2B). This indicates that Tpm3.1 is not recruited to granules in the absence of actin filaments and that Tpm3.1 forms a co-polymer with actin.

Further inside the gland, there was only partial inhibition of actin filament formation (evident in Fig. 2A), resulting in patches of

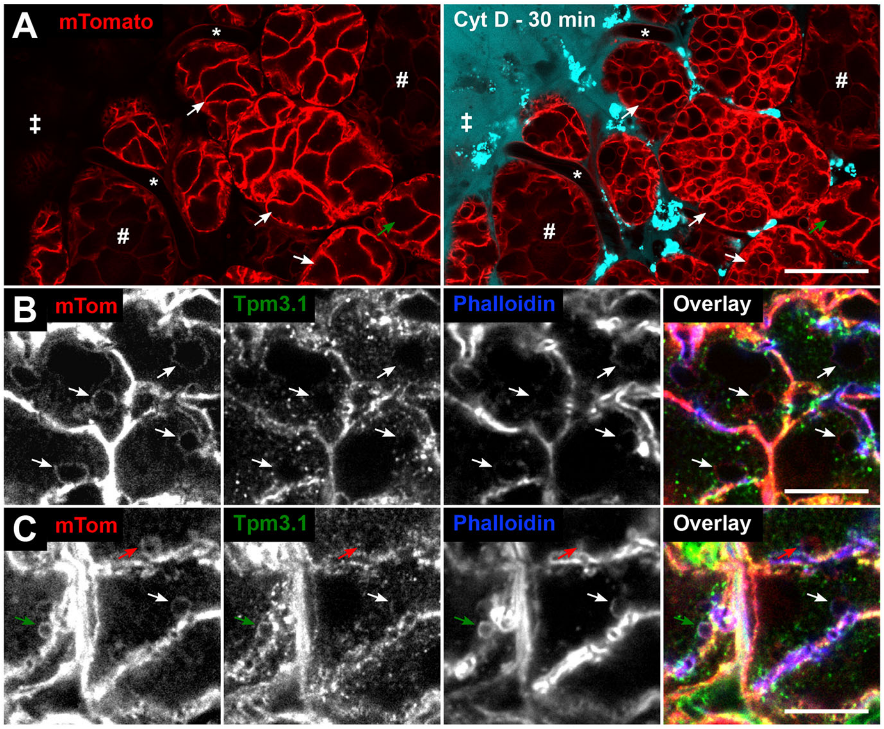

Fig. 2. Tpm3.1 recruitment onto fused granules is dependent on actin filaments. (A) Overview of intravital imaging of cytochalasin D (CytD) treatment of salivary glands in mTomato mice [stroma (‡), intact capillaries (*), ducts (#)]. Snapshots of glands before (left) and 30 min after (right) CytD treatment. The drug solution contained 10 kDa Alexa Fluor 647 dextran (cyan). CytD treatment for 30 min results in the formation of large vacuoles in acini (white arrows indicate the same acini pre- and post-CytD). CytD penetrance is not uniform, as shown by an unaffected acinus (green arrow) further from the edge of the organ. Enrichment of bright dextran puncta represent rapid dextran marker uptake by the resident stromal cells, such as dendritic cells and fibroblasts. Scale bar: 20 µm. (B,C) Detection of mTomato, Tpm3.1 and actin (phalloidin) on fused granules (arrows) in a salivary gland section of an mTomato mouse treated with CytD (10 min), followed by isoproterenol injection (10 min). (B) CytD-affected granules are enlarged (arrows) and largely devoid of both Tpm3.1 and F-actin staining. (C) The impact of CytD is variable, with some granules exhibiting full (red arrow) or no (green arrow) impact on the actin scaffold. The white arrow shows a fused granule with partial recruitment (crescent-like patch) of F-actin and Tpm3.1. Scale bars: 10 µm.

F-actin localising on granule membranes (Fig. 2C). Comparison with Tpm3.1 staining shows co-incidence of phalloidin and Tpm3.1 staining on such partially inhibited granules (white arrow in Fig. 2C). This is consistent with Tpm3.1 depending on actin filament formation to assemble on the granule surface and Tpm3.1 forming a co-polymer with actin *in vivo*.

Tpm3.1-knockout (KO) mice (Vlahovich et al., 2009) were stimulated with isoproterenol and their glands were stained with phalloidin. Phalloidin staining of granules was not affected by the absence of Tpm3.1 (Fig. S2A,B). This indicates that Tpm3.1 is not required for actin filament assembly on the granules; although, we cannot rule out a role for other Tpm isoforms. Indeed, antibody staining of fixed salivary gland sections revealed the presence of Tpm4.2 (an isoform of TPM4) on the apical plasma membrane and the granules (Fig. S1D).

Generation of a Tpm3.1–mNeonGreen KI mouse

In order to examine the behaviour of the endogenous Tpm3.1 protein in real time, CRISPR-Cas9 was used to introduce the mNeonGreen (NG) tag (Shaner et al., 2013) into the C-terminus of the gene encoding Tpm3.1 (Fig. 3). The mice were fertile and transmitted the tagged allele at a similar frequency to the endogenous allele, and PCR products of mouse DNA confirmed the presence of the wild-type (WT) and knock-in (KI) alleles (Fig. 3C). Western blots of Tpm3.1–NG mouse embryo fibroblasts (MEFs) showed that Tpm3.1–NG accumulates at levels <10% of WT Tpm3.1 (Fig. 3D). Tpm3.1–NG-expressing MEFs displayed a similar pattern of Tpm3.1–NG localization to that seen with anti-Tpm3.1 staining of WT MEFs (Fig. 3E,F; Fig. S2E). Intravital microscopy of the salivary glands of a Tpm3.1–NG KI mouse crossed to a Lifeact–RFP transgenic mouse showed that there was apical enrichment of Tpm3.1–NG (Fig. 3G, arrowheads) and localisation to fused secretory granules (arrows) characteristic of endogenous Tpm3.1 in acinar cells (Fig. 2B and C). Thus, the tagged gene product can incorporate with fidelity into actin filament bundles, but is either synthesised at a lower rate or is more rapidly turned over than the WT product.

The Tpm3.1–NG KI mouse shows similar recruitment kinetics for actin and Tpm3.1

The progeny of the Tpm3.1–NG and Lifeact–RFP mouse cross were used to visualise and quantify *de novo* assembly of actin and endogenous Tpm3.1. Tpm3.1–NG and Lifeact–RFP exhibit parallel accumulation on the granules during the first few seconds of granule fusion (Fig. 4A; Movie 2). Measurements for 16 granule-fusion events from multiple animals were averaged and the kinetics for the two tags were compared (Fig. 4C). Full kinetics are shown in Fig. S3A,B. The first significant Lifeact signal increase above baseline was detected at 965 ms, the same time point at which the first significant increase in Tpm3.1 signal was registered (Fig. 4C). This further suggests that the initiation of actin polymerisation and the co-assembly of Tpm3.1 are near-simultaneous.

Myosin IIA recruitment kinetics lag behind those of actin and Tpm3.1

Tpm3.1 has been shown to recruit myosin IIA (the form of non-muscle myosin II with its heavy chain encoded by *Myh9*) to stress fibres in neuroblastoma cells (Bryce et al., 2003), and myosin IIA and IIB (non-muscle myosin II with its heavy chain encoded by *Myh10*) isoforms have recently been shown to be recruited to salivary gland granules (Milberg et al., 2017). Interestingly, Tpm3.1 genetic ablation did not affect endogenous myosin IIA localisation on fused granules in mouse salivary gland acinar cells (Fig. S2C,D). We therefore focused on the kinetics of myosin IIA recruitment, and the temporal relationship with actin and Tpm3.1 recruitment in wild-type animals. To compare myosin IIA–GFP (GFP-tagged MYH9) with Tpm3.1–NG kinetics, we first established that at the same imaging parameters, the two tags yield similar signal intensity (Fig. S3C). Myosin IIA is recruited to granules that are positive for Lifeact–RFP (Fig. 4B; Fig. S4A); however, Lifeact was found on all

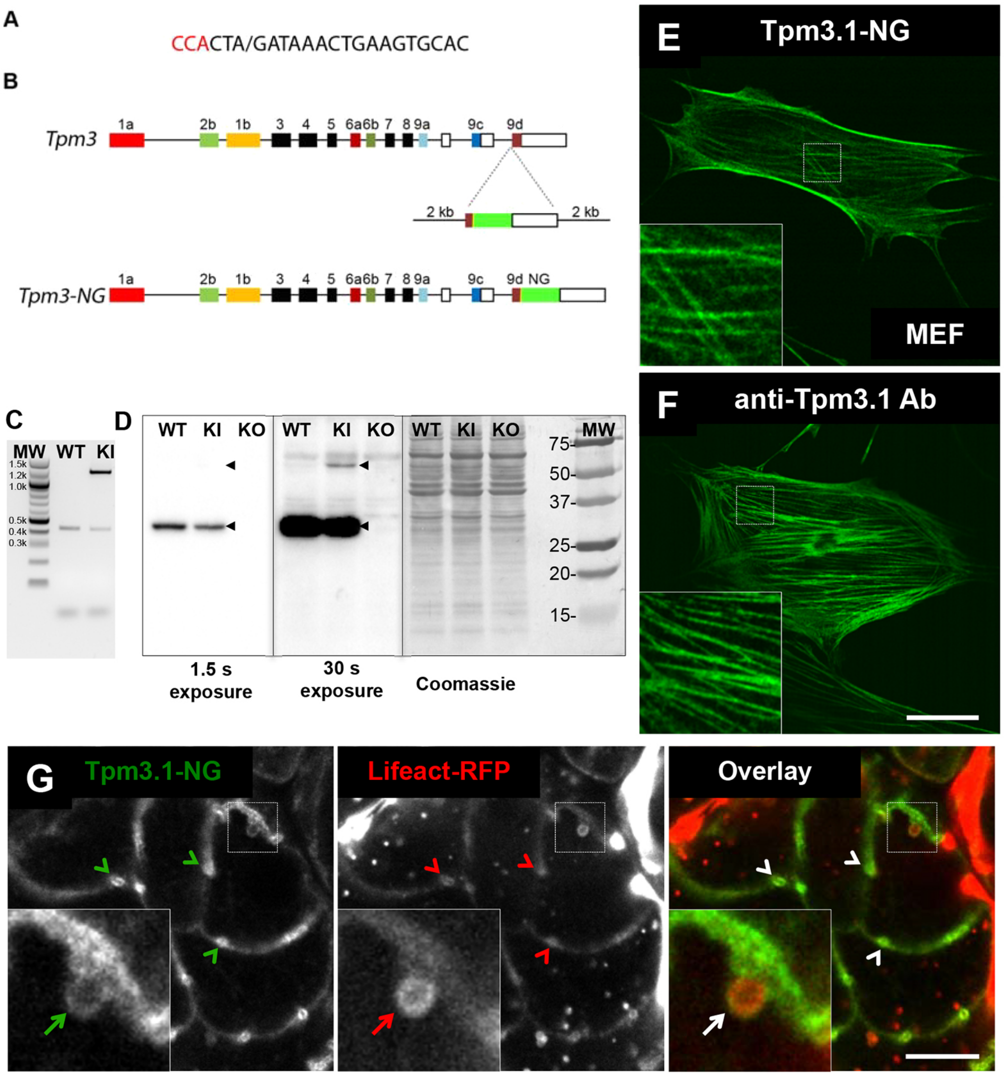

Fig. 3. Generation of Tpm3.1–mNeonGreen KI mouse. (A,B) The design strategy used to create fluorescently tagged KI mice via CRISPR. (A) Guide RNA used with the PAM site in red and the cut site marked with '/'. (B) Structure of the *Tpm3* gene. (C) Agarose gel showing PCR products using DNA extracted from WT and hemizygous KI mice as a template. (D) Western blots from MEF cells isolated from WT, Tpm3.1–NG KI and Tpm3.1 KO mice. The major product is detected by anti-Tpm3.1 antibody at ∼30 kDa in WT and KI lanes, and not in the KO lane. The KI product of ∼57 kDa is only detected after 30 s exposure. Wild-type and fusion protein Tpm3.1 bands are indicated with black arrowheads. Coomassie staining was used as a loading control (right panel). Molecular mass standards (MW) are shown in kDa. (E,F) MEF cells from Tpm3.1-NG KI and WT mice. (E) Confocal image of Tpm3.1–NG localised to stress fibres (inset) in Tpm3.1–NG KI MEF cells. (F) Confocal image of Tpm3.1 localised to stress fibres (inset) in WT MEF cells detected by anti-Tpm3.1 antibody. Scale bar: 20 µm. (G) Snapshot of a single acinus from the progeny of a Tpm3.1–NG mouse crossed with a Lifeact–RFP mouse, imaged with intravital confocal microscopy after injection of isoproterenol. Cortical distribution and enrichment of Tpm3.1–NG (green) and actin filaments marked by Lifeact (red) at APM/canaliculi is evident (arrowheads). The inset shows a fused granule (white arrow) that is enveloped by an F-actin scaffold (red arrow) containing Tpm3.1 filaments (green arrow). Scale bar: 10 µm; the width of the insets is 6.5 µm.

granules before myosin IIA (compare panels in Fig. 4B; Movie 3). Averaged binding curves for Lifeact–RFP and myosin IIA–GFP are shown in Fig. 4D. Full kinetics are shown in Fig. S4B,C. Lifeact–RFP and myosin IIA–GFP show very different kinetics, unlike Lifeact and Tpm3.1, indicating slower recruitment of myosin IIA than of Lifeact (Fig. 4D). Evaluation of the early time points revealed a 1.2 s gap between the first significant increase in Lifeact and myosin IIA signals (Fig. 4D). Differences in kinetics between Lifeact–RFP and myosin IIA–GFP were also supported by line scan analysis of example fusion events (Figs S3C, S4D). A similar lag between initial actin filament formation and myosin II recruitment on fused granules has been shown in the salivary glands of mice (Milberg et al., 2017) and in *Drosophila* larvae (Tran et al., 2015).

Assembly of actin, Tpm3.1 and myosin IIA on secretory granule membranes

Based on our measurements, we draw the following conclusions: (1) incorporation of Tpm3.1 depends on actin assembly, whereas in contrast actin assembles with the same kinetics regardless of the presence of Tpm3.1, (2) rapid Tpm3.1 incorporation into filaments occurs shortly after actin filaments are first detected (within 240 ms), (3) myosin IIA recruitment lags behind that of Tpm3.1 and (4) actin and Tpm3.1 have very similar initial recruitment kinetics whereas myosin IIA has comparatively slow initial recruitment kinetics. Taken together, these observations point to a process in which, shortly after actin polymerisation commences, Tpm3.1 co-assembles onto these actin filaments, and this is

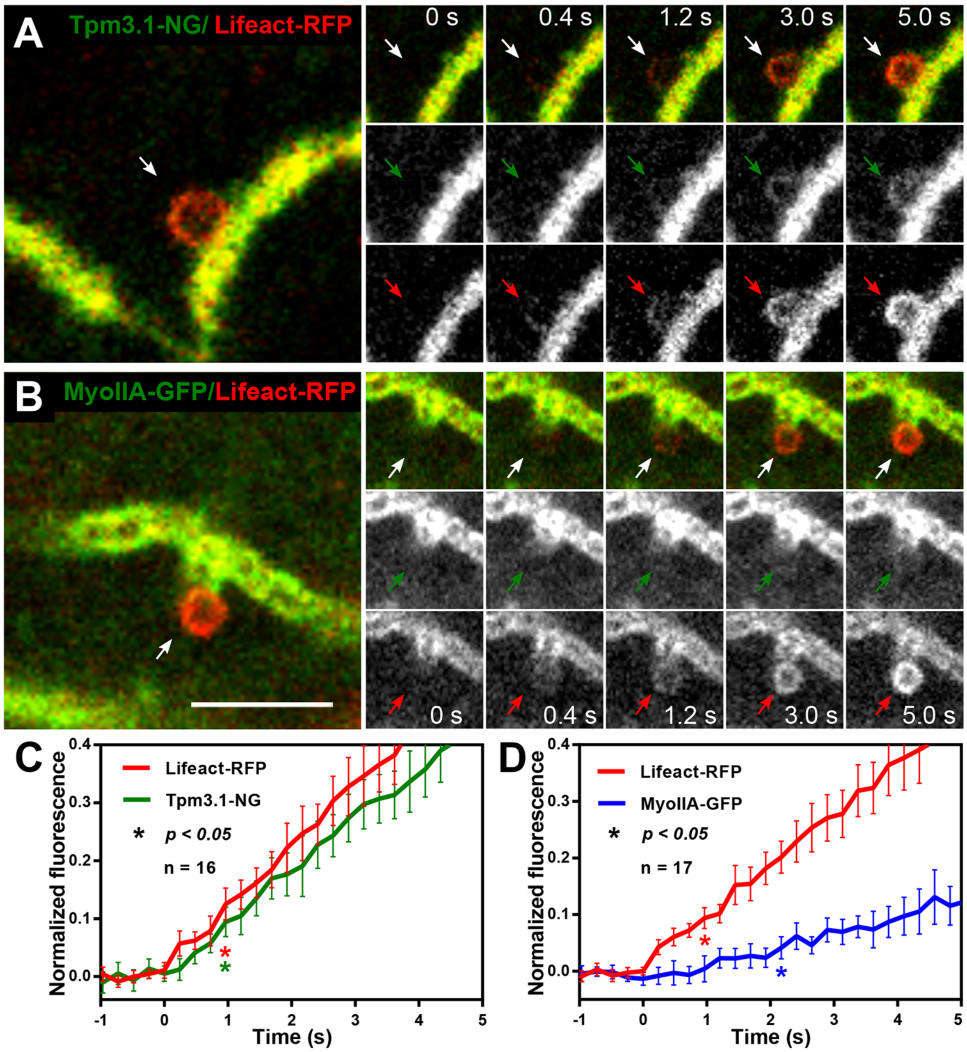

Fig. 4. The initial actin and Tpm3.1 filament assembly exhibits a close temporal relationship, unlike what is seen with myosin IIA. (A) Live intravital confocal imaging of *de novo* cytoskeleton assembly after isoproterenol-stimulated secretory granule fusion in the progeny of a Tpm3.1–NG KI and Lifeact-RFP mouse cross. The snapshot (left) shows a fused secretory granule (white arrow) near the APM/canaliculus. The image sequence (right) shows the progression of Tpm3.1–NG (green arrows) and Lifeact–RFP (red arrows) localisation over time. See also Movie 2. (B) Snapshot of intravital confocal imaged salivary acini *in situ* in the progeny of a myosin IIA–GFP KI and Lifeact–RFP mouse cross (left) after isoproterenol injection. Time-lapse sequence (right) showing the progression of actomyosin scaffold assembly around the granule with F-actin (red arrows) and myosin IIA (green arrows) localisation over time. See also Movie 3.
(C) Recruitment kinetics of Lifeact–RFP and Tpm3.1–NG acquired at 241 ms intervals shown as mean normalised fluorescence ±95% CI for each time point. An average of 16 fusion events from four mice were plotted. The first significant ($P<0.05$) increase in fluorescence intensity versus the zero time point was determined by one-way ANOVA and Dunnett's multiple comparison test for Lifeact–RFP (red asterisk, $P=0.0025$) and Tpm3.1–NG (green asterisk, $P=0.0215$).
(D) Recruitment kinetics of Lifeact–RFP (red line) and myosin IIA (blue line) acquired at 241 ms intervals are shown as normalised mean fluorescence intensities ±95% CI from 17 fusion events in four mice. The first significant ($P<0.05$) increase in fluorescence intensity versus the zero time point was determined, as in Fig. 4C, for Lifeact–RFP (red asterisk, $P=0.0283$) and myosin IIA (blue asterisk, $P=0.0091$). Scale bar: 5 µm; the width of the insets is 6.16 µm.

followed later by recruitment of the myosin IIA motor. During the very early stages of the process, new filaments in the structure surrounding the granule are being nucleated and grow in length.

It has been suggested that the actin filament forms first and then Tpm is added to the actin template (Holmes and Lehman, 2008; Wegner, 1979). Several research groups have shown that Tpm will nucleate at multiple sites along a single actin filament (Alioto et al., 2016; Christensen et al., 2017; Nicovich et al., 2016; Schmidt et al., 2015). However, because Tpm3.1 binds to six actin monomers in mammals, there is only a one in six chance that multiple Tpm3.1 nucleation events would join with each other 'in register' as they extend along the actin, resulting in gaps in Tpm3.1 coverage. This problem is resolved if Tpm3.1 is added to the pointed end (Hsiao et al., 2015) of growing actin filaments shortly after their nucleation and continues to co-polymerise with actin as the filament is extended. The observation that formin nucleators regulate Tpm incorporation into actin filaments (Alioto et al., 2016; Johnson et al., 2014; Tojkander et al., 2011) is compatible with such a proposal.

MATERIALS AND METHODS

Animals

Animal experiments were performed in accordance with the NSW Animal Research Act (1985) and Australian National Health and Medical Research Council (NHMRC) 'Code' 8th edition (2013). All experiments were approved by the UNSW Sydney Animal Care and Ethics Committee under applications 14/92A and 17/100B. Male mice (*Mus musculus*) aged 8–24 weeks were used in this study. Mice were sourced as described below, and colonies were maintained at the Australian BioResources Facility (Moss Vale, NSW, Australia) and allowed to acclimatise for 1 week prior to experimentation. Animals were housed in specific pathogen-free, humidity- and temperature-controlled facilities, under a 12 h:12 h light:dark cycle, and provided standard laboratory chow and water *ad libitum*. Tpm3.1 knock-out (KO) mice were previously generated in house (Vlahovich et al., 2009). Tpm3.1 KO mice lack the 9d exon of the *Tpm3* gene and are unable to make the Tpm3.1 and Tpm3.2 isoforms. mTomato mice have been described previously (Muzumdar et al., 2007). All tissues in these mice express tandem dimer tomato fluorescent protein (tdTomato) fused to the plasma membrane (PM)-targeting peptide from MARCKS, making this a PM reporter mouse line (Masedunskas et al., 2011). The mTomato mouse strain was purchased from Jackson Laboratory (Bar Harbor, ME, USA) and used alone or in a cross to Lifeact–GFP mice in a homozygous state. Lifeact–GFP and Lifeact–RFP transgenic mice were a gift from Roland Wedlich-Soldner (Riedl et al., 2010) and were used in crosses in a hemizygous state. Myosin IIA–GFP knock-in (KI) mice were generated as described (Zhang et al., 2012) and used in Lifeact–RFP crosses in a homozygous state. The genotypes of the mice were confirmed by PCR, as described in the original publications. Tpm3.1 from the endogenous locus was C-terminally tagged with mNeonGreen (NG) in a mouse line using CRISPR at the South Australia Genome Editing Facility (SAGE, University of Adelaide, Australia). Target sites near Tpm3 exon 9d were identified using the MIT CRISPR Design Tool (Ran et al., 2013). One high-scoring guide RNA (gRNA) sequence was selected that cut at the 5′ intron–exon boundary of exon 9d (CCACTA/GATAAACTGAAGTGCAC; / indicates the cut site). The plasmid repair template was synthesised by GeneArt (Thermo Fisher Scientific, Waltham, MA) and consisted of 2 kb homology arms flanking a mutated PAM site (TCA), exon 9d and a 10 amino acid linker (GGGGSGGGGS), and the NG sequence (a gift from Jiwu Wang, Department of Photobiology and Bioimaging, The Scintillon Institute, San Diego, CA, USA) (Shaner et al., 2013) inserted in frame with exon 9d (Fig. 3). The Tpm3.1–NG construct has been validated by analysing ectopic expression in mouse embryonic fibroblasts (Appaduray et al., 2016). The T in the PAM site was selected as the mutation as it is preferable for splicing efficiency (Dogan et al., 2007). C57Bl/6 mouse zygote pronuclei were injected with Cas9 mRNA (25 ng/µl), CRISPR guide RNA (10 ng/µl) and circular plasmid donor. Surviving zygotes were transferred to pseudopregnant female recipients and the resulting pups were screened for homologous integration of the donor template by PCR using genomic DNA extracted from ear biopsy samples using forward PCR primer, 5′-TCCTTGCAACTGGAGCAAGTC-3′, and reverse PCR primer, 5′-TGCATTGAAGACACTGCGTTG-3′. Hemizygous Tpm3.1–NG KI mice (C57Bl/6 background) were used for experiments and to generate a cross with Lifeact–RFP mice in a hemizygous state. The animals were genotyped by PCR (Fig. 3C) using forward primer, 5′-CAGTAGGCAAGCCAGAG-ACC-3′, and reverse primer, 5′-CCAACTGGAACTCTGGGAAA-3′, resulting in a 1143 bp band for the KI allele and 403 bp band for the WT allele. New England Biolabs (Ipswich, MA) 100 bp DNA Ladder was used to confirm the size of the bands. The presence of the Tpm3.1–NG protein was confirmed by western blotting and *in situ* fluorescence microscopy (Fig. 3).

Cell culture and immunofluorescence staining

Mouse embryo fibroblasts (MEFs) were isolated from day 14.5 C57Bl/6 WT, Tpm3.1 KO and Tpm3.1–NG KI mouse embryos and cultured as previously described (Tojkander et al., 2011). Cells were grown in Dulbecco's modified Eagle's medium (DMEM) with 10% (v/v) fetal bovine serum (FBS) at 37°C and 5% CO_2. To visualise Tpm3.1–NG localization, KI MEFs were fixed in 4% paraformaldehyde (PFA) at room temperature (RT) for 15 min and washed in PBS three times. For immunofluorescence staining, WT MEFs at passages 1–3 were seeded into Fluorodish tissue culture dishes (World Precision Instruments Pty Ltd, Hitchin, UK) and grown to 70–90% confluence. Cells were fixed in 4% PFA at RT for 15 min, permeabilised in cold methanol for 15 min, washed in PBS and blocked in 2% BSA in PBS at RT for 60 min. Cells were incubated with CG3 star 635 antibody 1:250 in PBS at RT for 1 h. CG3 Star 635 mouse monoclonal antibody (Novy et al., 1993) conjugated to an Abberior-635 dye recognises the 1b exon from the TPM3 gene. Cells were washed 3 times with PBS, mounted with Immuno-Mount (Thermo Fisher Scientific) and imaged using a Nikon A1 inverted scanning confocal microscope fitted with a Nikon Plan Apochromat lambda series 60×/1.4 NA oil immersion objective. CG3 Star 635 (emission wavelength 654 nm) was excited with a 640 nm laser. mNeonGreen fluorescent protein (emission wavelength 517 nm) was excited with a 488 nm laser.

Western blotting

Cell lysates were made from WT, Tpm3.1 KO and Tm3.1–NG KI MEFs in RIPA buffer and analysed by SDS-PAGE and western blotting, as described previously (Tojkander et al., 2011). Protein concentration was determined by using the Pierce BCA Protein Assay Kit (Thermo Fisher Scientific). Equal amounts of protein (20 µg) were separated on a 12% SDS-PAGE gel and electro-transferred to PVDF membranes. Membranes were incubated with blocking buffer and 5% skimmed milk powder in TBS (100 mM Tris-HCl, pH 7.5, 150 mM NaCl). Tpm 3.1 was recognised by using monoclonal antibody CG3 (1:200 in blocking buffer) (Tojkander et al., 2011) and secondary antibody rabbit anti-mouse IgG antibody-conjugated to horseradish peroxidase (Abcam) (1:10,000 in blocking buffer). The primary antibody was incubated overnight and the secondary antibody was incubated for 2 h, followed by 4×15 min washes in PBS. Blots were developed with the Luminata Crescendo Western HRP Substrate (Millipore), and 1–120 s exposures were taken via the Chemidoc Imaging System (Bio-Rad Laboratories). Protein loading was examined by staining the protein gel blots with 0.1% (w/v) Coomassie Brilliant Blue R350, 20% (v/v) methanol and 10% (v/v) acetic acid.

Tissue sectioning and staining

Fixed sucrose-infused frozen sections (Figs 1 and 2) were made as follows. Adult male C57Bl/6 mice were anaesthetised by intraperitoneal injection of 100 mg/kg body weight ketamine and 15 mg/kg body weight xylazine. Exocytosis of secretory granules was stimulated by subcutaneous injection of 0.01 mg/kg body weight isoproterenol for 10 min. In some experiments, surgically externalised salivary glands (SGs) were locally treated with 10 µM cytochalasin D 10 min prior to exocytosis stimulation. A drug solution was prepared by dissolving in pre-warmed (37°C) saline, which was then added dropwise onto the SGs for the duration of the experiment; 10 min after isoproterenol injection, SGs were excised, immersed in 2% PFA at RT for 1 h and transferred into 15% sucrose overnight. Sucrose-infused tissues were placed in plastic tissue moulds in Tissue-Tek O.C.T. and frozen in isopentane cooled in liquid nitrogen. Then, 10 µm sections were cut (Cryostat, Leica CM1950) and incubated with blocking buffer (5% goat serum, 5% FBS, 1% BSA in PBS) at RT for 1–2 h. Mouse mAb 2G10 (1:2.5 in blocking buffer), which recognises the 9d exon from the *Tpm3* gene (Tpm3.1 and 3.2 isoforms) (Tojkander et al., 2011), was added at RT for 12 h, and then secondary antibodies conjugated to Alexa Fluor 488 (mouse; Invitrogen) (1:750 in blocking buffer) with either phalloidin labelled with Atto-647N (ATTO-TEC) or TRITC (Sigma-Aldrich) (1:250 in blocking buffer) were added at RT for 1–2 h. Tpm4.2 and myosin IIA were detected with delta9d rabbit polyclonal (1:100 dilution; Millipore, AB5449) and myosin IIA (1:100 dilution; Covance, PRB-440P), respectively. Images were taken with an Olympus FV1000 laser scanning confocal microscope equipped with an UPLAN 60×/1.35 NA oil immersion objective at 100 nm/pixel spatial sampling density. For granule overlap scoring, a Nikon A1 laser scanning confocal microscope equipped with a CFI Plan Apochromat lambda series 60×/1.4 NA oil immersion objective was used. Seven *z*-slices were taken every 200 nm sampling over 1.2 µm depth at 120 nm/pixel spatial sampling density. Fused granules were identified in the phalloidin channel as spherical structures with a diameter of 0.5–1.6 µm that were connected to the APM that lines the canaliculi. They were then scored for the presence of Tpm3.1 as detected by 2G10 antibody staining (Table S1).

Intravital microscopy

Mice (18–34 g) were anaesthetised by intraperitoneal injection of 100 mg/kg body weight ketamine and 15 mg/kg body weight xylazine, SGs were surgically externalised and prepared for subcellular intravital microscopy as described (Masedunskas et al., 2013, 2011). The SG was stabilised onto a coverslip on a microscope stage with the vasculature and the innervation still intact. Intravital imaging was performed using a Nikon A1 inverted laser scanning confocal microscope fitted with a CFI Plan Apochromat lambda series 60×/1.27 NA water immersion objective, an Okolab humidified temperature-controlled microscope enclosure, objective heater and a custom-made stage insert. Animal body and SG temperatures were monitored with a MicroTherma T2 thermometer equipped with rectal and thin implantable probes (Braintree Scientific) and heating was adjusted to maintain the temperature at 37–38°C. GFP and NG were excited with a 488 nm laser, and RFP and tdTomato were excited with a 561 nm laser. For time-lapse imaging, frames were acquired in sequential mode at 943 ms/frame (Fig. 1) or 241 ms/frame (all other figures) at a spatial sampling density of 140 nm per pixel. An imaging plane with a visible APM/canaliculus was selected as close to the surface of the organ as possible – at a depth of 8-12 µm. During imaging, any noticeable drift was manually corrected in the *x*, *y* or *z* dimension. For some experiments, 10 µM cytochalasin D was prepared by mixing it with pre-warmed saline [with or without 2 mg/ml Alexa Fluor 647-conjugated 10 kDa dextran (Thermo Fisher Scientific)] and perfused over the surface of the gland at 3 µl/min during the imaging using a PHD Ultra Nanomite programmable syringe pump (Harvard Apparatus). Exocytosis of secretory granules was stimulated by subcutaneous injection of 0.01 mg/kg body weight isoproterenol.

Image quantification and statistics

Images were taken using NIS Elements software. Image processing and data extraction was performed by using ImageJ/Fiji (Schindelin et al., 2012) and Metamorph (Molecular Devices) software. When necessary, drift and motion correction on time-lapse image stacks was carried out with the StackReg ImageJ plugin (Thevenaz et al., 1998). To extract fluorescence trace data from single-granule fusion events, a circular region of interest (ROI) with a diameter of 15 pixels was drawn over the image area capturing the exocytosis event. Only exocytosis events fully captured for the first 20–30 s in the focal plane and devoid of drift, motion artefacts and signal contribution from additional objects, such as plasma membrane, were included in the analysis. Integrated pixel fluorescence intensity values from the ROI were extracted and transferred to Microsoft Office Excel for processing as separate channels. Time t=0 for all events was taken as the time point preceding the first significant increase in Lifeact fluorescence above the baseline value. The baseline or background values for each channel were calculated by averaging ∼5 s worth of data points preceding an increase in fluorescence. The fluorescence intensity values may vary between mice or cells; therefore, the granule fluorescence traces were normalised individually by first subtracting the calculated average baseline value for each trace and then expressing the result as fractional values, with one being the maximum and zero being the minimum/background value. The maximum fluorescence value was picked for each trace and channel by using the MAX function in Excel, which returns the largest value from a sequence of numbers. Separate granule exocytosis events of a given data set were then synchronised to time t=0 with respect to Lifeact fluorescence and plotted from 10 s before the initiation of Lifeact signal increase until 70 s after t=0, when the fluorescence intensity returns to baseline (Figs S3,S4). Mean intensity values±95% CI were calculated and plotted by using Graphpad Prism 7 (GraphPad Software) in Fig. 4. Mean intensity values at each time point were analysed by one-way ANOVA, and the first time point exhibiting a significant increase (P<0.05) in fluorescence was identified with a Dunnett's multiple comparison test of each time point versus the zero time point. A total of 16 or 17 granule fusion events from four animals were quantified. Line scan analysis was performed across fusing granules over time (Figs S3C and S4D). A 3 µm line was drawn across each granule in the raw images and the average (over two pixels) fluorescence intensities in the red and green channels were recorded along the line in Metamorph software. Images for the figures were adjusted for contrast and brightness in Metamorph or ImageJ to have an optimal display range for features of interest, such as secretory granules, and then converted into RGB images. In some cases, the adjustment for secretory granule visualisation may have resulted in unavoidable dynamic range 'clipping' of the brightest secondary features such as basolateral PM. The images were then assembled into final figures using Inkscape software (The Inkscape Project). Supplementary figures were assembled in Microsoft PowerPoint software and exported to PDF format.

Acknowledgements

We thank the UNSW BioMedical Imaging Facility (BMIF) under the direction of Renee Whan for help with the microscopy and the UNSW Biological Resource Centre under the direction of Stephen Danon. We thank Michael Carnell for microscopy and image analysis advice.

Competing interests

The authors declare no competing or financial interests.

Author contributions

Conceptualization: A.M., P.W.G., E.C.H.; Methodology: A.M., R.W., P.W.G., E.C.H.; Validation: A.M., M.A.A.; Investigation: A.M., M.A.A., C.A.L., M.L.C., M. Heydecker, M. Holliday, J.C.M.M.; Resources: J.H., M.W., P.T., Y.Z., R.S.A., N.S.B., P.W.G., E.C.H.; Writing - original draft: A.M., P.W.G.; Writing - review & editing: A.M., T.B., R.W., N.S.B., P.W.G., E.C.H.; Supervision: A.M., A.K., T.M., P.W.G., E.C.H.; Funding acquisition: A.M., P.W.G., E.C.H.

Funding

This work was supported by grants to P.W.G. and E.C.H. from the Australian National Health and Medical Research Council (APP1079866 and APP1100202), to E.C.H., A.M. and R.W. from the Australian Research Council (DP160101623), and to P.W.G., E.C.H., A.M. and M.A.A. from The Kid's Cancer Project.

Supplementary information

Supplementary information available online at http://jcs.biologists.org/lookup/doi/10.1242/jcs.212654.supplemental

References

Alioto, S. L., Garabedian, M. V., Bellavance, D. R. and Goode, B. L. (2016). Tropomyosin and profilin cooperate to promote formin-mediated actin nucleation and drive yeast actin cable assembly. *Curr. Biol.* **26**, 3230-3237.

Appaduray, M. A., Masedunskas, A., Bryce, N. S., Lucas, C. A., Warren, S. C., Timpson, P., Stear, J. H., Gunning, P. W. and Hardeman, E. C. (2016). Recruitment kinetics of tropomyosin Tpm3.1 to actin filament bundles in the cytoskeleton is independent of actin filament kinetics. *PLoS ONE* **11**, e0168203.

Bovellan, M., Romeo, Y., Biro, M., Boden, A., Chugh, P., Yonis, A., Vaghela, M., Fritzsche, M., Moulding, D., Thorogate, R. et al. (2014). Cellular control of cortical actin nucleation. *Curr. Biol.* **24**, 1628-1635.

Bryce, N. S., Schevzov, G., Ferguson, V., Percival, J. M., Lin, J. J., Matsumura, F., Bamburg, J. R., Jeffrey, P. L., Hardeman, E. C., Gunning, P. et al. (2003). Specification of actin filament function and molecular composition by tropomyosin isoforms. *Mol. Biol. Cell* **14**, 1002-1016.

Christensen, J. R., Hocky, G. M., Homa, K. E., Morganthaler, A. N., Hitchcock-DeGregori, S. E., Voth, G. A. and Kovar, D. R. (2017). Competition between Tropomyosin, Fimbrin, and ADF/Cofilin drives their sorting to distinct actin filament networks. *eLife* **6**, e23152.

Cooper, J. A. (1987). Effects of cytochalasin and phalloidin on actin. *J. Cell Biol.* **105**, 1473-1478.

Dogan, R. I., Getoor, L., Wilbur, W. J. and Mount, S. M. (2007). Features generated for computational splice-site prediction correspond to functional elements. *BMC Bioinformatics* **8**, 410.

Goins, L. M. and Mullins, R. D. (2015). A novel tropomyosin isoform functions at the mitotic spindle and Golgi in Drosophila. *Mol. Biol. Cell* **26**, 2491-2504.

Gunning, P. W., Ghoshdastider, U., Whitaker, S., Popp, D. and Robinson, R. C. (2015a). The evolution of compositionally and functionally distinct actin filaments. *J. Cell Sci.* **128**, 2009-2019.

Gunning, P. W., Hardeman, E. C., Lappalainen, P. and Mulvihill, D. P. (2015b). Tropomyosin - master regulator of actin filament function in the cytoskeleton. *J. Cell Sci.* **128**, 2965-2974.

Holmes, K. C. and Lehman, W. (2008). Gestalt-binding of tropomyosin to actin filaments. *J. Muscle Res. Cell Motil.* **29**, 213-219.

Hsiao, J. Y., Goins, L. M., Petek, N. A. and Mullins, R. D. (2015). Arp2/3 complex and cofilin modulate binding of tropomyosin to branched actin networks. *Curr. Biol.* **25**, 1573-1582.

Jang, Y., Soekmadji, C., Mitchell, J. M., Thomas, W. G. and Thorn, P. (2012). Real-time measurement of F-actin remodelling during exocytosis using Lifeact-EGFP transgenic animals. *PLoS ONE* **7**, e39815.

Johnson, M., East, D. A. and Mulvihill, D. P. (2014). Formins determine the functional properties of actin filaments in yeast. *Curr. Biol.* **24**, 1525-1530.

Lazarides, E. (1975). Tropomyosin antibody: the specific localization of tropomyosin in nonmuscle cells. *J. Cell Biol.* **65**, 549-561.

Lazarides, E. (1976). Actin, alpha-actinin, and tropomyosin interaction in the structural organization of actin filaments in nonmuscle cells. *J. Cell Biol.* **68**, 202-219.

Masedunskas, A., Sramkova, M., Parente, L., Sales, K. U., Amornphimoltham, P., Bugge, T. H. and Weigert, R. (2011). Role for the actomyosin complex in regulated exocytosis revealed by intravital microscopy. *Proc. Natl. Acad. Sci. USA* **108**, 13552-13557.

Masedunskas, A., Appaduray, M., Hardeman, E. C. and Gunning, P. W. (2013). What makes a model system great? A case for intravital microscopy for studying the actin cytoskeleton. *IntraVital* **2**, e26287.

Miklavc, P., Hecht, E., Hobi, N., Wittekindt, O. H., Dietl, P., Kranz, C. and Frick, M. (2012). Actin coating and compression of fused secretory vesicles are essential for surfactant secretion–a role for Rho, formins and myosin II. *J. Cell Sci.* **125**, 2765-2774.

Miklavc, P., Ehinger, K., Sultan, A., Felder, T., Paul, P., Gottschalk, K.-E. and Frick, M. (2015). Actin depolymerisation and crosslinking join forces with myosin II to contract actin coats on fused secretory vesicles. *J. Cell Sci.* **128**, 1193-1203.

Milberg, O., Shitara, A., Ebrahim, S., Masedunskas, A., Tora, M., Tran, D. T., Chen, Y., Conti, M. A., Adelstein, R. S., Ten Hagen, K. G. et al. (2017). Concerted actions of distinct nonmuscle myosin II isoforms drive intracellular membrane remodeling in live animals. *J. Cell Biol.* **216**, 1925-1936.

Muzumdar, M. D., Tasic, B., Miyamichi, K., Li, L. and Luo, L. (2007). A global double-fluorescent Cre reporter mouse. *Genesis* **45**, 593-605.

Nicovich, P. R., Janco, M., Sobey, T., Gajwani, M., Obeidy, P., Whan, R., Gaus, K., Gunning, P. W., Coster, A. C. F. and Böcking, T. (2016). Effect of surface chemistry on tropomyosin binding to actin filaments on surfaces. *Cytoskeleton* **73**, 729-738.

Nightingale, T. D., White, I. J., Doyle, E. L., Turmaine, M., Harrison-Lavoie, K. J., Webb, K. F., Cramer, L. P. and Cutler, D. F. (2011). Actomyosin II contractility expels von Willebrand factor from Weibel-Palade bodies during exocytosis. *J. Cell Biol.* **194**, 613-629.

Novy, R. E., Sellers, J. R., Liu, L.-F. and Lin, J. J.-C. (1993). In vitro functional characterization of bacterially expressed human fibroblast tropomyosin isoforms and their chimeric mutants. *Cell Motil. Cytoskeleton* **26**, 248-261.

Panzer, L., Trube, L., Klose, M., Joosten, B., Slotman, J., Cambi, A. and Linder, S. (2016). The formins FHOD1 and INF2 regulate inter- and intra-structural contractility of podosomes. *J. Cell Sci.* **129**, 298-313.

Porat-Shliom, N., Milberg, O., Masedunskas, A. and Weigert, R. (2013). Multiple roles for the actin cytoskeleton during regulated exocytosis. *Cell. Mol. Life Sci.* **70**, 2099-2121.

Ran, F. A., Hsu, P. D., Wright, J., Agarwala, V., Scott, D. A. and Zhang, F. (2013). Genome engineering using the CRISPR-Cas9 system. *Nat. Protoc.* **8**, 2281-2308.

Riedl, J., Flynn, K. C., Raducanu, A., Gärtner, F., Beck, G., Bösl, M., Bradke, F., Massberg, S., Aszodi, A., Sixt, M. et al. (2010). Lifeact mice for studying F-actin dynamics. *Nat. Methods* **7**, 168-169.

Schindelin, J., Arganda-Carreras, I., Frise, E., Kaynig, V., Longair, M., Pietzsch, T., Preibisch, S., Rueden, C., Saalfeld, S., Schmid, B. et al. (2012). Fiji: an open-source platform for biological-image analysis. *Nat. Methods* **9**, 676-682.

Schmidt, W. M., Lehman, W. and Moore, J. R. (2015). Direct observation of tropomyosin binding to actin filaments. *Cytoskeleton* **72**, 292-303.

Shaner, N. C., Lambert, G. G., Chammas, A., Ni, Y., Cranfill, P. J., Baird, M. A., Sell, B. R., Allen, J. R., Day, R. N., Israelsson, M. et al. (2013). A bright monomeric green fluorescent protein derived from Branchiostoma lanceolatum. *Nat. Methods* **10**, 407-409.

Sokac, A. M., Co, C., Taunton, J. and Bement, W. (2003). Cdc42-dependent actin polymerization during compensatory endocytosis in Xenopus eggs. *Nat. Cell Biol.* **5**, 727-732.

Thevenaz, P., Ruttimann, U. E. and Unser, M. (1998). A pyramid approach to subpixel registration based on intensity. *IEEE Trans. Image Process.* **7**, 27-41.

Tojkander, S., Gateva, G., Schevzov, G., Hotulainen, P., Naumanen, P., Martin, C., Gunning, P. W. and Lappalainen, P. (2011). A molecular pathway for myosin II recruitment to stress fibers. *Curr. Biol.* **21**, 539-550.

Tran, D. T., Masedunskas, A., Weigert, R. and Ten Hagen, K. G. (2015). Arp2/3-mediated F-actin formation controls regulated exocytosis in vivo. *Nat. Commun.* **6**, 10098.

Vlahovich, N., Kee, A. J., Van der Poel, C., Kettle, E., Hernandez-Deviez, D., Lucas, C., Lynch, G. S., Parton, R. G., Gunning, P. W. and Hardeman, E. C. (2009). Cytoskeletal tropomyosin Tm5NM1 is required for normal excitation-contraction coupling in skeletal muscle. *Mol. Biol. Cell* **20**, 400-409.

Wegner, A. (1979). Equilibrium of the actin-tropomyosin interaction. *J. Mol. Biol.* **131**, 839-853.

Yu, H.-Y. E. and Bement, W. M. (2007). Multiple myosins are required to coordinate actin assembly with coat compression during compensatory endocytosis. *Mol. Biol. Cell* **18**, 4096-4105.

Zhang, Y., Conti, M. A., Malide, D., Dong, F., Wang, A., Shmist, Y. A., Liu, C., Zerfas, P., Daniels, M. P., Chan, C.-C. et al. (2012). Mouse models of MYH9-related disease: mutations in nonmuscle myosin II-A. *Blood* **119**, 238-250.

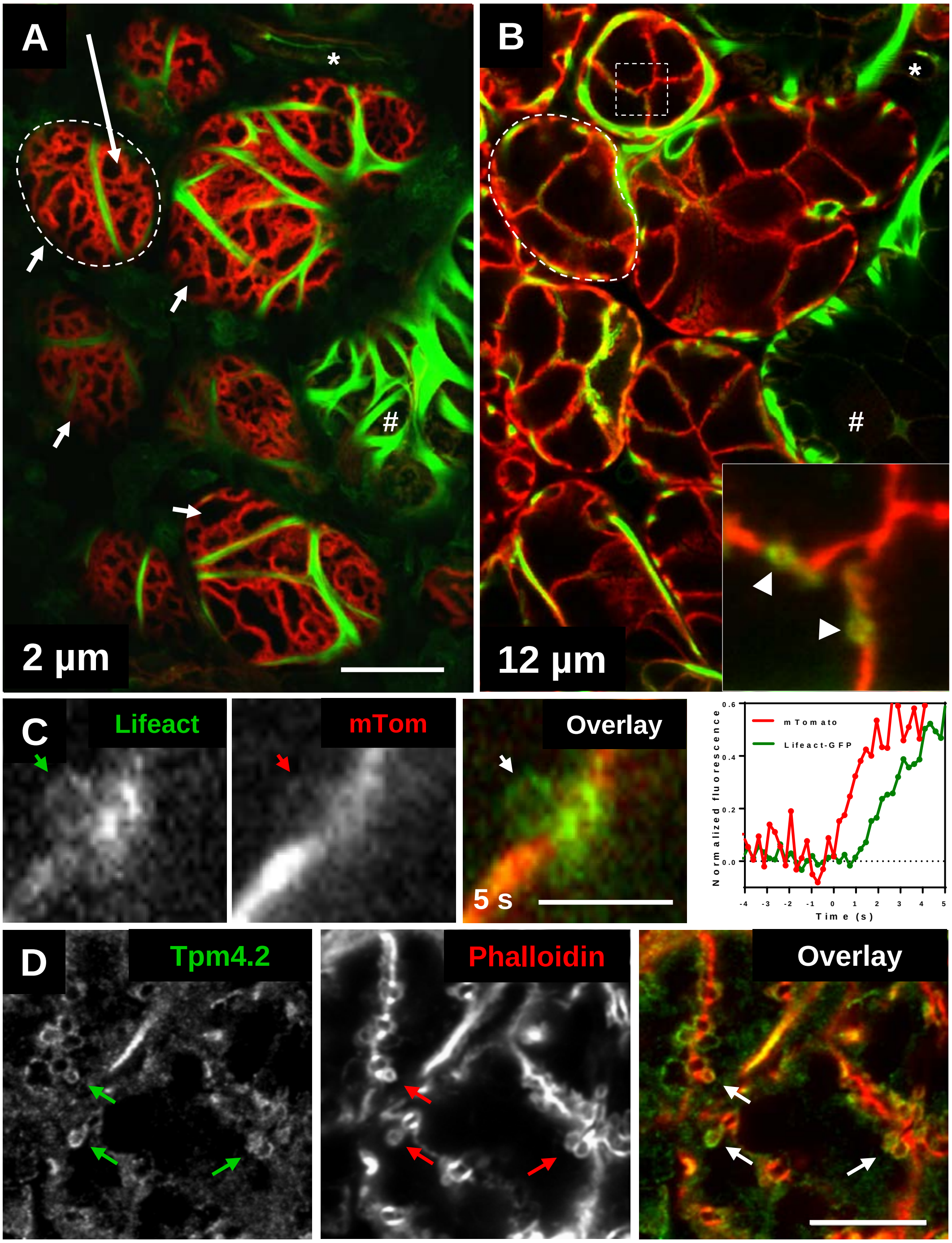
A
*
#
2 µm
B
*
#
12 µm
C
Lifeact
mTom
Overlay
5 s
mTomato
Lifeact-GFP
Normalized fluorescence
0.6
0.4
0.2
0.0
-4
-3
-2
-1
0
1
2
3
4
5
Time (s)
D
Tpm4.2
Phalloidin
Overlay

Figure S1. Actin is enriched on apical membranes in submandibular salivary glands. Tpm4.2 is present on the granules. Related to Figure 1. (A-B) Overview of submandibular salivary gland acinar cells in mTomato x Lifeact-GFP mice imaged with intravital confocal microscopy. Snapshots of salivary glands showing membrane marker mTomato (red) and F-actin marker Lifeact-GFP (green) taken at 2 or 12 µm depth [individual acini (arrows), blood vessels (*), ducts (#)]. Single acinus is outlined by dashed line. At the surface slice (A) mTomato delineates microridges of basolateral plasma membrane of acinar epithelial cells, while myoepithelial cells wrapping around the acini are seen as spindle-like structures enriched in green fluorescence. Inset in (B) shows a canaliculus cross-section showing APM enriched in F-actin (green, arrowheads). Scale bar is 20 µm and the inset width is 10.5 µm. (C) Example image and fluorescence trace from timelapse imaging of exocytosis in mTomato x Lifeact-GFP mice at 241 ms temporal resolution. Single frame at 5 s after the onset of actin polymerization is shown with fused granule visible in both channels (arrows). See also Fig1 C-D. Scale bar = 3 µm (D) Detection of Tpm4.2 and actin (TRITC-phalloidin) on fused granules (arrows) in fixed salivary gland section of wild-type mouse 10 min post isoproterenol injection. Scale bar = 10 µm.

	Granule overlap scores
Mouse1	181 / 183
Mouse2	244 / 244
Mouse3	200 / 203
Mouse4	185 / 185
Total	810 / 815

Table S1. Tpm3.1 and actin filaments co-localize on fused secretory granules in mouse submandibular salivary glands. Relates to Figure 1E. Isoproterenol-stimulated salivary glands from WT mice (n = 4) were collected, fixed and stained for F-actin and endogenous Tpm3.1. Quantification of phalloidin and Tpm3.1 overlap on fused granules is shown. Results are expressed as number of granules positive for both phalloidin and Tpm3.1 versus total granules scored. Five granules out of 815 were labeled with phalloidin and did not exhibit anti-Tpm3.1 antibody staining.

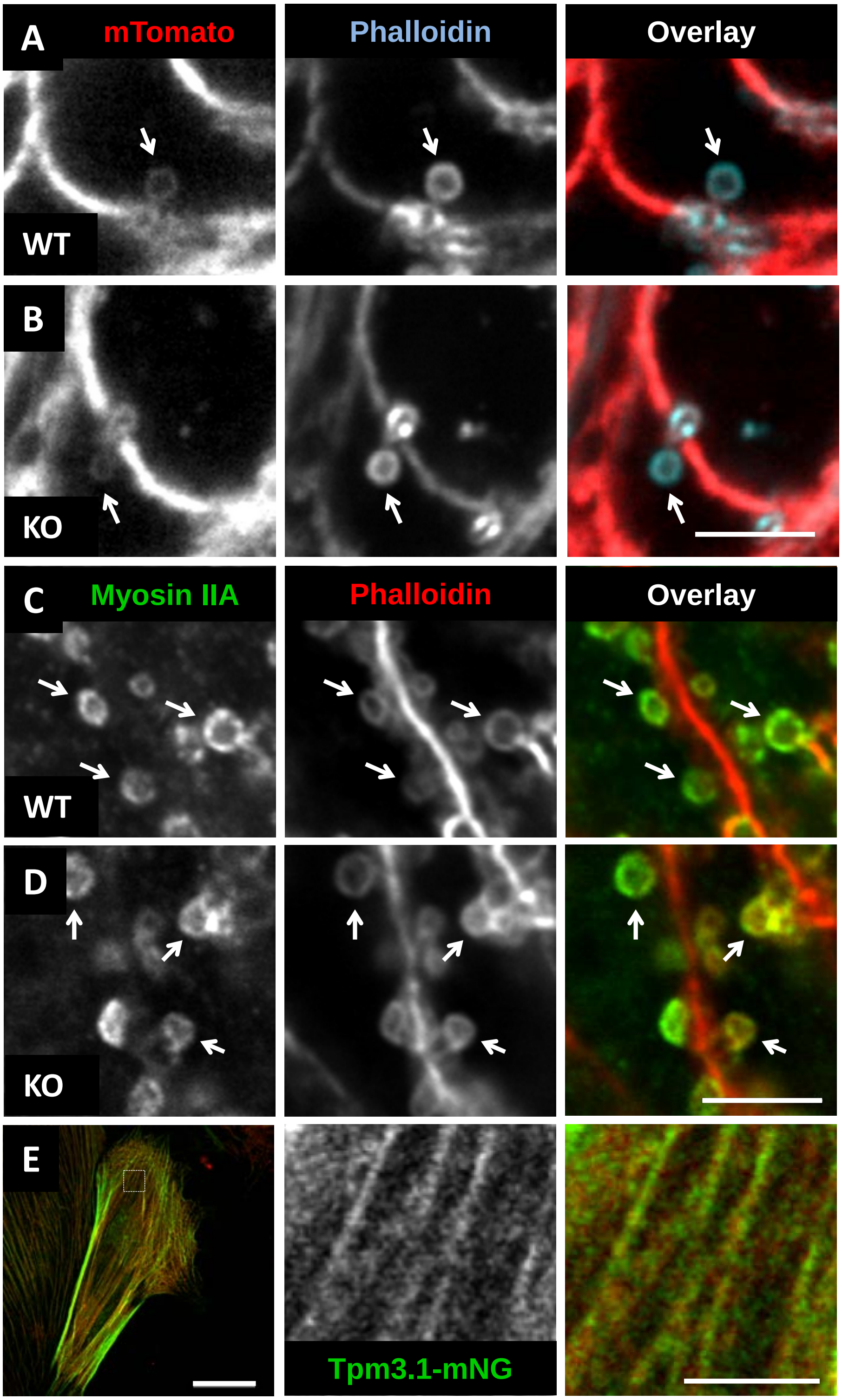
A
mTomato
Phalloidin
Overlay
WT
B
KO
C
Myosin IIA
Phalloidin
Overlay
WT
D
KO
E
Tpm3.1-mNG

Figure S2. F-actin coat assembly is independent of Tpm3.1 Relates to Figure 2. (A-B) Representative sections of salivary glands from (A) mTomato (WT) and (B) Tpm3.1 KO x mTomato (KO) mice after 5 min isoproterenol stimulation were stained for F-actin (Alexa647-phalloidin, cyan). Fused secretory granules are shown (arrows). No abnormalities in actin coat assembly on the granules were observed indicating that actin recruitment is not affected by the ablation of Tpm3.1. (C-D) Sections of salivary glands from (C) wild-type (WT) and (D) Tpm3.1 KO (KO) mice after 10 min isoproterenol stimulation were stained with anti-myosin IIA antibody (green) and TRITC-phalloidin (red). Fused secretory granules are visible (arrows). No obvious differences in myosin IIA recruitment on the granules were observed. Scale bars for panels A-D are 5 µm. (E) MEF cell isolated from Tpm3.1-NG KI mouse embryo, relates to Fig. 3. Confocal image of Tpm3.1-NG (green) and endogenous Tpm3.1 (red) detected by anti-Tpm3.1 antibody are localized onto stress fibers (right panels). Scale bar for the main image is 30 µm and 5 µm for the zoomed view.

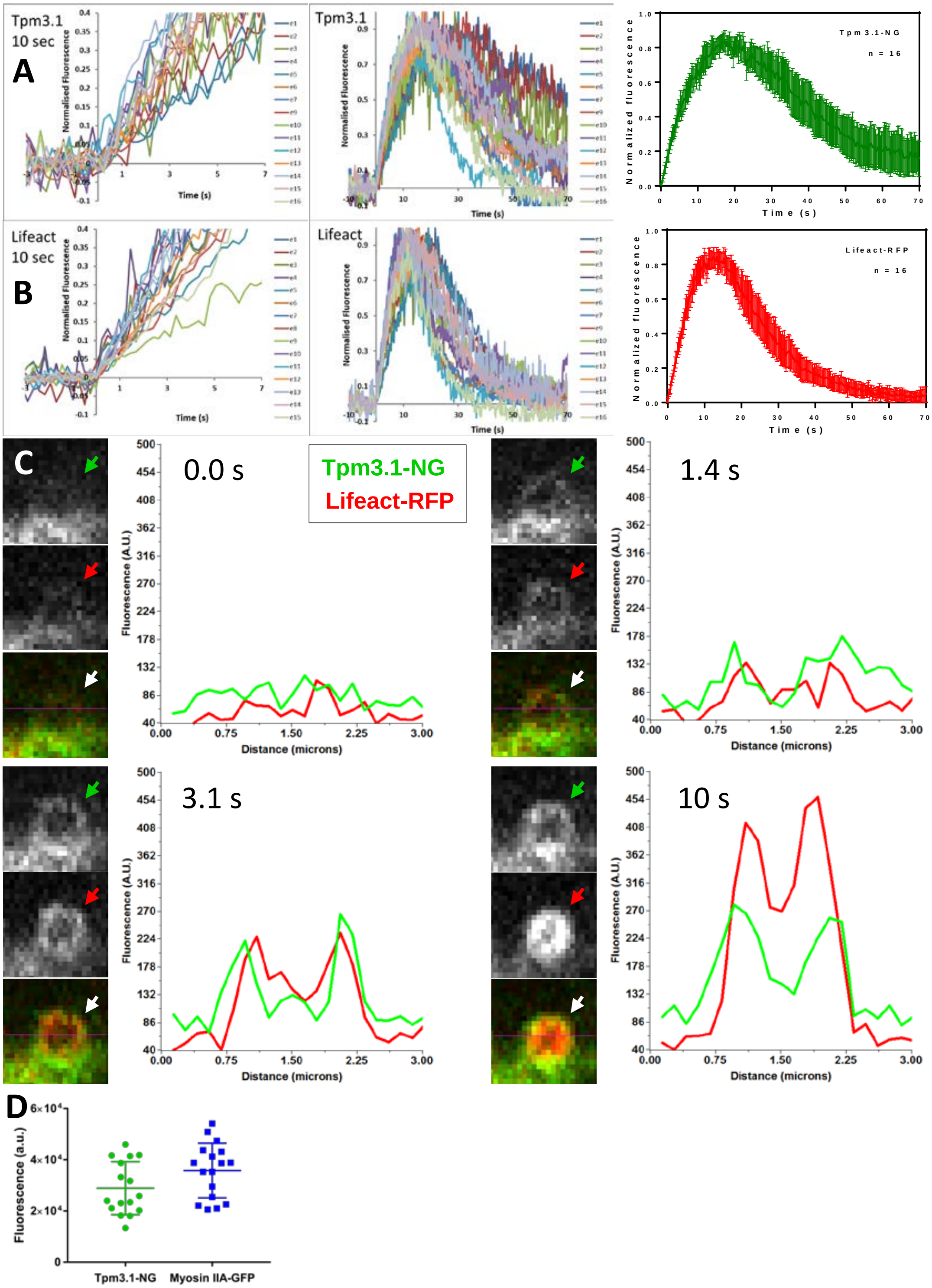
A
Tpm3.1
10 sec
Normalised Fluorescence
Time (s)
Tpm3.1
Normalised Fluorescence
Time (s)
e1
e2
e3
e4
e5
e6
e7
e8
e9
e10
e11
e12
e13
e14
e15
e16
Tpm3.1-NG
n = 16
Normalized fluorescence
Time (s)
B
Lifeact
10 sec
Normalised Fluorescence
Time (s)
Lifeact
Normalised Fluorescence
Time (s)
Lifeact-RFP
n = 16
Normalized fluorescence
Time (s)
C
0.0 s
1.4 s
3.1 s
10 s
Tpm3.1-NG
Lifeact-RFP
Fluorescence (A.U.)
Distance (microns)
D
Fluorescence (a.u.)
Tpm3.1-NG
Myosin IIA-GFP

Figure S3. Normalised fluorescence intensity traces of Tpm3.1NG and Lifeact-RFP recruitment kinetics from multiple secretory granule fusion events. Related to Figure 4. (A-B) Live intravital confocal was performed to capture *de novo* cytoskeleton assembly after isoproterenol-stimulated secretory granule fusion in Tpm3.1-NG KI x Lifeact-RFP mouse. Data were recorded in time-lapse mode at a rate of 241 ms per frame. Fluorescence intensity profiles were acquired by drawing a small region of interest around fusing granules. Normalised fluorescence traces of Tpm3.1-NG (A) and Lifeact-RFP (B) for 16 granule fusion events are shown. Fusion events were synchronised by setting one frame before Lifeact-RFP fluorescence increase above baseline as t = 0 s. Fluorescence traces spanning 10 s and 70 s are shown, with mean normalized intensities +/- 95% CI of all traces presented in rightmost panels. (C) Line scan (line shown in magenta in the overlay images) fluorescence intensity plots and corresponding images from a single secretory granule fusion in Tpm3.1-NG KI (green arrows) x Lifeact-RFP (red arrows) mouse. Four timepoints from the acquisition sequence are shown. Images were captured at 140 nm per pixel spatial and 241 ms per frame temporal resolution. Image width and line length are 3 µm. (D) Using identical imaging parameters, time-lapse images were acquired of MyoIIA-GFP KI x Lifeact-RFP mice. To compare the brightness of the Tpm3.1-NG and MyoIIA-GFP raw maximal fluorescence intensity values for each granule were plotted as mean +/- SD. The fluorescence reached maximum on the granules between 20-40 seconds after fusion. Student’s t-test revealed no significant difference between the means (p = 0.068).

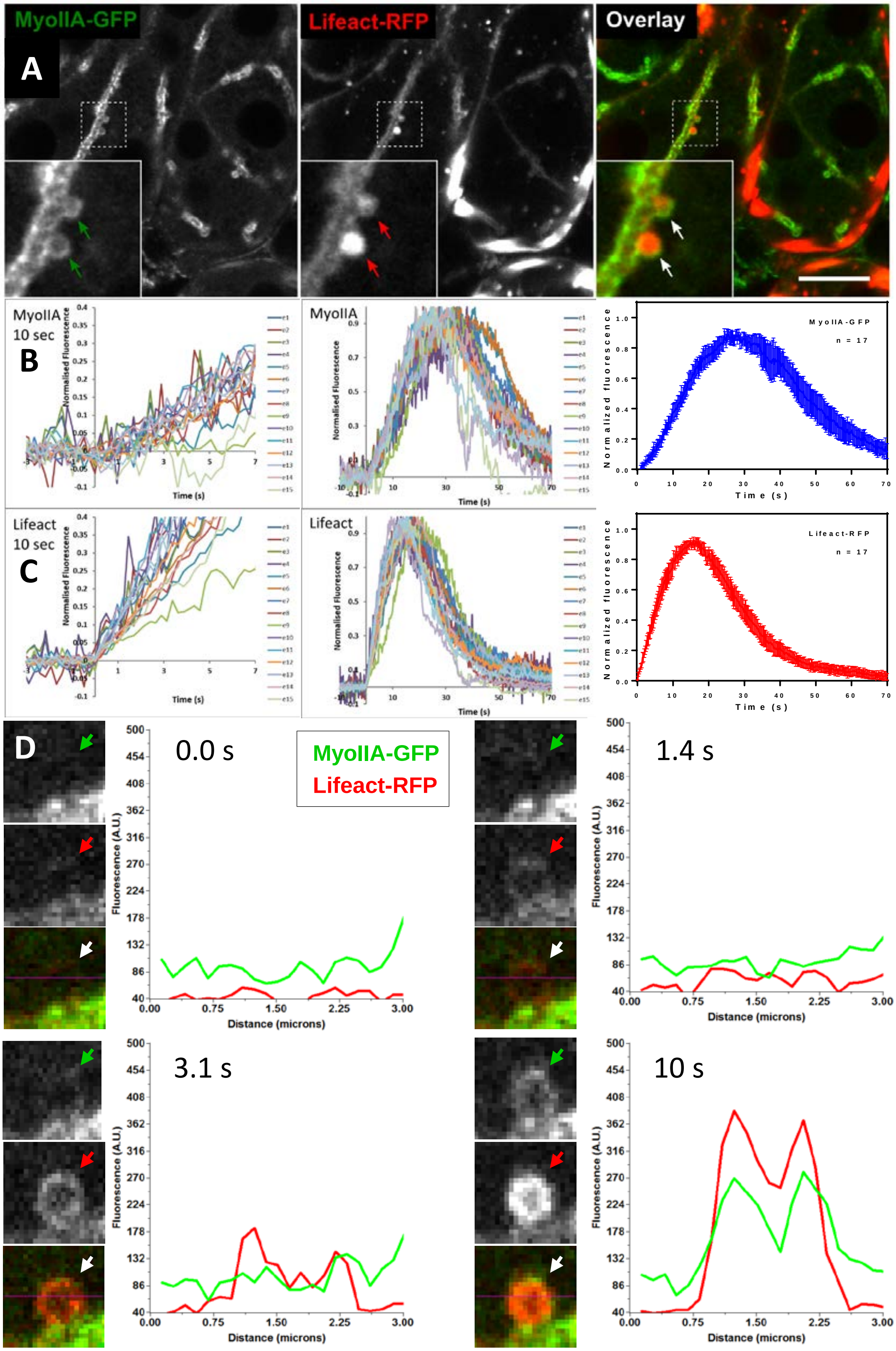
A
MyoIIA-GFP
Lifeact-RFP
Overlay
B
MyoIIA
10 sec
Normalised Fluorescence
Time (s)
MyoIIA
Normalised Fluorescence
Time (s)
e1 e2 e3 e4 e5 e6 e7 e8 e9 e10 e11 e12 e13 e14 e15
Normalized fluorescence
Time (s)
MyoIIA-GFP
n = 17
C
Lifeact
10 sec
Normalised Fluorescence
Time (s)
Lifeact
Normalised Fluorescence
Time (s)
Normalized fluorescence
Time (s)
Lifeact-RFP
n = 17
D
0.0 s
1.4 s
3.1 s
10 s
MyoIIA-GFP
Lifeact-RFP
Fluorescence (A.U.)
500 454 408 362 316 270 224 178 132 86 40
Distance (microns)
0.00 0.75 1.50 2.25 3.00

Figure S4. MyoIIA-GFP KI mouse cross with Lifeact-RFP images and normalised fluorescence intensity traces from multiple secretory granule fusion events. Related to Figure 4. (A) Snapshots of intravital confocal imaged salivary acini in situ in MyoIIA-GFP KI x Lifeact-RFP mice. Both F-actin and Myosin IIA are enriched at the canaliculi/ APM of acinar cells. Inset shows 2 fused granules (arrows) with recruitment of actin and Myosin IIA onto the granules after exocytosis is stimulated by isoproterenol. Scale bar is10 µm and the width of the insets is 6.5 µm. (B-C) Normalised fluorescence traces of MyoIIA-GFP (B) and Lifeact-RFP (C) for 17 granule fusion events are shown. Fluorescence traces spanning 10 s and 70 s are shown, with mean normalized intensities +/- 95% CI of all traces presented in rightmost panels. (D) Line scan (line shown in magenta) fluorescence intensity plots and corresponding images from a single secretory granule fusion in myosin IIA KI (green arrows) x Lifeact-RFP (red arrows) mouse. Four timepoints from acquisition sequence are shown. Images were captured at 140 nm per pixel spatial and 241 ms per frame temporal resolution. Image width and line length are 3 µm.

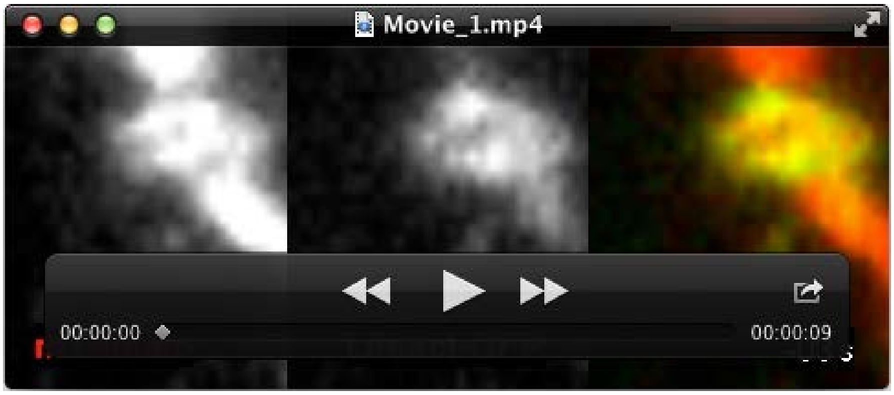

Movie 1. Actin filaments form a scaffold around secretory granules after fusion with the apical plasma membrane in mouse salivary acinar cells in vivo. Related to Figures 1A-D and S1C.

Intravital confocal imaging of actin filament assembly during isoproterenol-stimulated secretory granule exocytosis in submandibular salivary gland acinar cells in an mTomato x Lifeact-GFP mouse. A close-up view of a single exocytosis event is shown with granule membrane marked by mTomato (red) and actin filaments labeled by Lifeact-GFP (green). Time zero is set to one frame first appearance of Lifeact-GFP signal on the secretory granule. Contrast and brightness was adjusted in each channel for optimal visualization of the granule at early stage post-fusion. Time-lapse image frames were acquired at 944 ms intervals and playback was set to 7.5 frames per sec (approximately 7.8 x real time). Time is displayed in seconds. Scale bar = 3 µm.

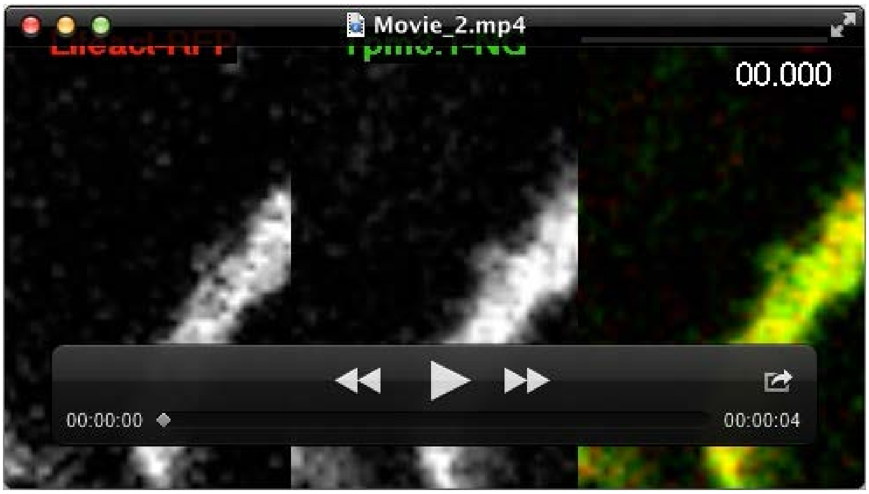

Movie 2. Initial actin and Tpm3.1 filaments simultaneously assemble around fused secretory granules in mouse acinar cells in vivo. Related to Figures 4A and S3.
Intravital confocal imaging of actin filament assembly during secretory granule exocytosis in submandibular salivary gland acinar cells in Tpm3.1-NG KI x Lifeact-RFP mouse. Single exocytosis event acquired at higher temporal resolution (241 ms image frame intervals) is shown. Tpm3.1-NG (green) and Lifeact-RFP (red) appear to be recruited simultaneously around the granule. Time zero is set to one frame prior to first appearance of Lifeact-RFP signal on the secretory granule. Playback was set to 60 frames per sec (approximately 16x real time). Time is displayed in seconds.milliseconds. Scale bar = 5 µm.

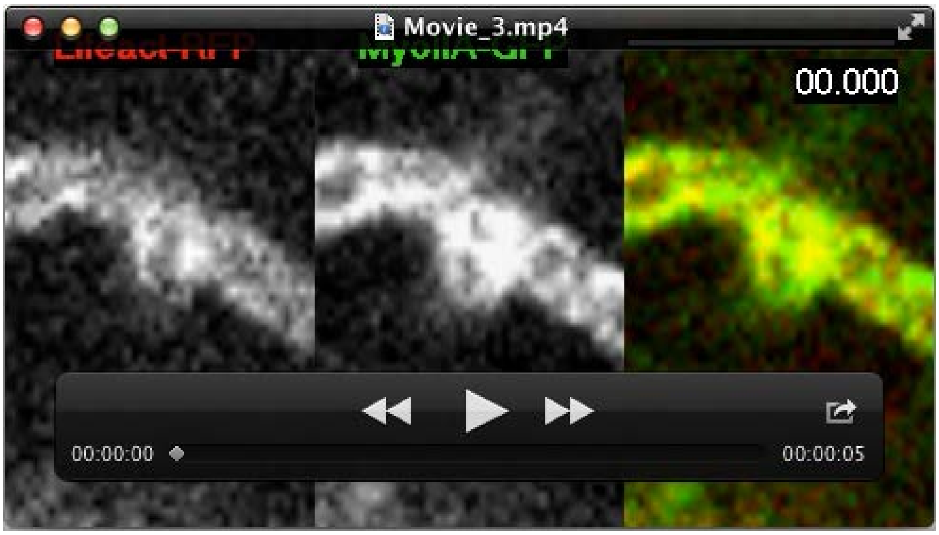

Movie 3. Myosin IIA-GFP recruitment follows Initial actin filament assembly around fused secretory granules in mouse acinar cells in vivo. Related to Figures 4B and S4.
Intravital confocal imaging of actin filament assembly during secretory granule exocytosis in submandibular salivary gland acinar cells in Myosin IIA-GFP KI x Lifeact-RFP mouse. Single exocytosis event acquired at higher temporal resolution (241 ms image frame intervals) is shown. The initial recruitment of Myosin IIA-GFP (green) around the granule seems to lag a few seconds behind the first appearance of Lifeact-RFP (red). Playback was set to 60 frames per sec (approximately 16x real time). Time is displayed in seconds.milliseconds. Scale bar = 5 µm.